CrossMark

SHORT PAPER

Phase portrait analysis for automatic initialization of multiple snakes for segmentation of the ultrasound images of breast cancer

Khwunta Kirimasthong[1] · Annupan Rodtook[2] · Utairat Chaumrattanakul[3] ·
Stanislav S. Makhanov[1]

Abstract Segmentation of ultrasound (US) images of breast cancer is one of the most challenging problems of modern medical image processing. A number of popular codes for US segmentation are based on the active contours (snakes) and on a variety of modifications of gradient vector flow. The snakes have been used to locate objects in various applications of medical images. However, the main difficulty in applying the method is initialization. Therefore, we suggest a new method for automatic initialization of active contours based on phase portrait analysis (PPA) of the underlying vector field and a sequential initialization of trial multiple snakes. The PPA makes it possible to exclude the noise and artifacts and properly initialize the multiple snakes. In turn, the trial snakes allow us to differentiate between the seeds initialized inside and outside the desired object. While preceding methods require the manual selection of at least one seed point inside the object or rely on the particular distribution of the gray levels, the proposed method is fully automatic and robust to the noise, as can be seen from the tests with synthetic and real images.

✉ Stanislav S. Makhanov
makhanov@siit.tu.ac.th

1   School of Information and Computer Technology, Sirindhorn
    International Institute of Technology, Thammasat University,
    Tiwanont Road, T. Bangkadi, A. Muang,
    Pathum Thani 12000, Thailand

2   Department of Computer Science, Ramkhamhaeng
    University, Bangkok 10240, Thailand

3   Department of Radiology, Faculty of Medicine, Thammasat
    University, 12, Khlong Luang, Pathum Thani 12120,
    Thailand

1 Introduction

Many segmentation methods have been developed for ultrasound (US) images of breast cancer. Numerous reviews (e.g., 1 [1, 2]) present methods to treat segmentation of medical images as a general image processing problem, while others use a priori information relevant to the specific type of the images. Conventional segmentation methods include thresholding [3–7], neural networks [8–15], mode-based methods (such as expectation–maximization) [16, 17], clustering [18, 19], region growing [20], deformable active contours (snakes) [3, 21–25] and level set methods [26]. The segmentation is usually followed by feature extraction to distinguish malignant and benign masses. The features include shape of the mass, posterior acoustic behavior, radial gradient or margin, variance/autocorrelation, contrast, distribution of the distortions and many others [27]. Survey [28] reports 17 texture features, 17 morphological features, 10 model-based features and 13 descriptor features.

Recent advances in the US segmentation include fusion of the medical images [29], using graphic processing units [30], multi-atlas segmentation [31], incorporating priors [32] using the AI methods combined with snakes [31, 33–35], advanced level set methods [36–43] and the multi-scale approach [44]. The US image analysis is a part of the computer-assisted diagnostic systems. The entire evaluation includes mammography (usually the primary step), thermography [45, 46], Doppler imagery [47, 48] and elasticity analysis [49]. Such evaluation along with the computerized cytology [50, 51] constitutes a basic architecture toward the ultimate goal of fully automatic clinical decision support systems for detection and grading of the breast cancer [52].

Active contours (snakes) originally introduced by Kass et al. [53] are one of the most popular techniques for extraction of complex objects from digital images. Since the seminal work of Kass and colleagues, active contours have been applied to many object extraction tasks with differing degrees of success (e.g., survey [54]). Further improvements process the underlying vector field which moves the snake toward the required boundary, such as the gradient vector flow (GVF) [55] and the generalized gradient vector flow field (GGVF) [56]. Some variations of these ideas are the multi-directional GGVF [57] and the nonlinear diffusion model [58]. Recent modifications are the convolution vector flow [59], Poisson gradient vector field [60, 61], segmented external force field [62], dynamic directional gradient vector flow [63], normal gradient vector field [64], priory directional information vector flow [65], adaptive diffusion flow [66], multi-feature gradient vector flow [67] and divergence gradient vector flow [68].

A competing approach called the level set method (LSM) [69] is based on the ideas proposed by Osher and Sethian [70] to use a model of propagating liquid interfaces with curvature-dependent speeds. The LSM combined with the contour energy minimization resulted in a variety of the so-called geodesic deformable models [71–74]. However, the LSM makes it difficult to impose arbitrary geometric or topological constraints on the evolving contour via the higher-dimensional hypersurface. Besides, the level set models may generate shapes having inconsistent topology with respect to the actual object, when applied to noisy images characterized by large boundary gaps [75] and non-closed curves [62]. Besides, the LSM is computationally expensive since it requires to propagate a 2D object (the level set surface) in the 3D space, whereas the active contour methods evolve a 1D object (the closed contour) in the 2D space.

Numerous research papers apply the active contours to medical images. The examples are multi-directional snakes: skin cancer images [57], topology-adaptive snakes: MR brain images and CT scans [76], gravitational force snakes: a variety of medical and non-medical images [77], narrow-band snakes: MRI and CT scan images of lungs [78], distance snake [79], GVF snake, balloon snake [80], "area and length" snakes [72], geodesic snakes [71], constrained snakes [73] and level set method: MRI, CT and US images of brain, liver and kidney [74], region-competition snakes (originally [81]): CT scan slices of arteries [82], sectored snakes [83]: abdominal CT scans [84], parametric snakes: US of breast masses [85], 3D snakes: US breast cancer images [22, 85], GVF snakes with an edge map preprocessing: US of the kidney tumors [86], GVF snakes combined with the region growing and the median filter: US breast tumors [87], sketch snakes [22]: chest X-ray images [22], combination of snakes and active shape models: US of the human heart [88], the early vision and the discrete snakes: the US images [89], multi-resolution snake: echographic and echobrachial images [90], GGVF snakes combined with a continuous force field analysis: breast tumors in the US images [91] and geodesic snakes and coupled geometric snakes: female pelvic organs in the MRI images [92–94].

The success of such segmentations critically depends on preprocessing and initial positions (initialization) of the snakes. Noise and small objects may attract the snake to a local energy minimum, which does not correspond to the actual boundary. Therefore, to reach the desired boundary, the initial contour should be initialized close to the object. The problem can be partially solved by initializing multiple snakes, which can split, merge and collapse (disappear). Moreover, the higher-order active contours (quadratic snakes) proposed by Rochery et al. [95] are able to "see" each other, so that they do not intersect if not required. However, such strategies still require proper initialization.

It is often critical to differentiate the snakes initialized inside and outside the object. Obviously, if one can do it for every position in the image, it means that the object has already been segmented. However, the algorithm should only do it for some points for which such differentiation is possible. One of the possible solutions is based on growing snakes initialized around false objects and false edges so that they do not get attracted to them during their evolution (Fig. 1c).

Unfortunately, up to now only a few papers deal with the snake initialization. For instance, [62] segments the external force field, to divide the image domain into disjoint regions. The snakes can be individually initialized within each of the enclosures and moved to the targeted object boundary within it, avoiding being attracted by other objects. [96, 97] proposed a quasi-automated initialization method requiring only one user-defined point. The method employs the centers of divergence [98] combined with a tracing procedure to create a "skeleton" of the object, consisting of the points of strong and weak divergence. A contour constructed around the skeleton is usually inside the object and can be used as the initial seed. However, the method is not fully automated and still requires at least one user-defined point inside the object. Moreover, it can be shown that the skeleton can eventually grow outside the boundary of the object. In this case, the initialized snake evolves to false boundaries. Besides, [96] does not evaluate the performance of the method on a series of images and does not estimate an impact of the noise. Poisson gradient vector flow [61] is applied to automatic segmentations of positron emission tomography images of the liver. The initial contour is selected by Canny edge detection from the candidate curves selected by a genetic algorithm. The proposed initialization is not always reliable and may not
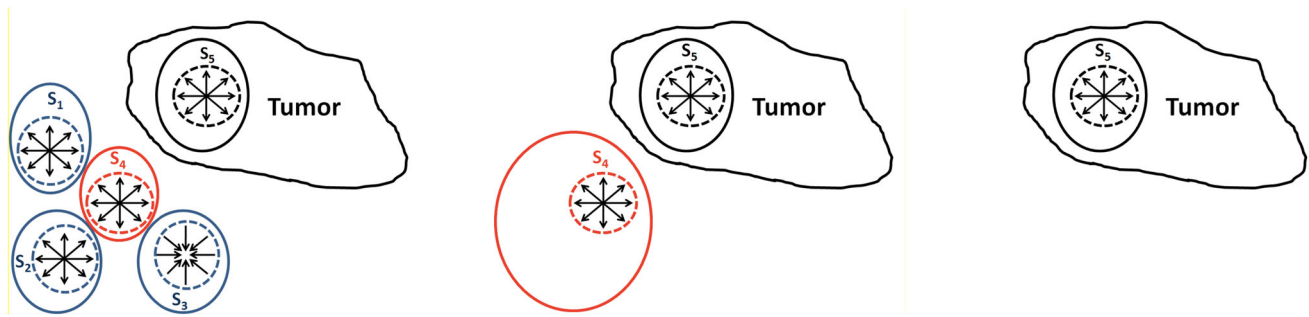
Fig. 1 Elimination of the external stars: **a** S_4 gets blocked, **b** S_1, S_2, S_3 are eliminated, **c** S_4 eliminated

work for multiple objects. However, the important idea of running trial initializations and getting some additional information from them has been introduced. Recently, these techniques have been applied to automatic extraction of face contours in images and video [99]. A similar idea of a "cascade of the active contours" has been proposed for the detection of the synovial boundaries in US images [100].

As far as the US images are concerned, the majority of the initialization methods are based on the analysis of the gray levels and textures, to locate the most probable seed points [21, 101, 102]. Saliency and feature maps, such as texture maps, have been recently applied for contour initialization in [103]. A hybrid vector field, combining the structure of the gradient vector flow and the texture, has been proposed in [104]. A "degraded" (simplified) Chan–Vese model [105] generates an initial contour in the framework of region-based segmentation. Several papers use priori knowledge about the typical position of a human organ in the US image (see, for instance, [106]). However, all the above methods depend on the particular features of the image and may not work if a strong noise is present. Besides, they do not use the advantages of multiple trial snakes. Therefore, this paper proposes a new algorithm for automatic initialization, which combines the idea of vector field analysis [98] and multiple competing active contours [61]. Our vector field analysis performed by the phase portrait method has been used in a variety of image processing applications, e.g., [107–113]. However, the use of PPA in the framework of initialization algorithms has been overlooked. Our proposed iterative procedure resolves the most common initialization problems. First, it decides whether the seed snake is inside or outside the object. Second, the procedure makes it possible to efficiently detect and avoid false boundaries and artifacts. The proposed algorithm has been tested against the initialization method [96, 97] on a series of synthetic and real ultrasound images of breast cancer. The numerical experiments show significantly improved reliability and accuracy. Besides, the proposed PPA has been tested against the adaptive

diffusion flow [66], a recent version of the level set method [37, 38] and an advanced fuzzy C-mean clustering [39, 40] with the seeds initialized manually *inside* the cancer tumor. The numerical experiments demonstrate that proposed technique outperforms the above algorithms even though we use the most basic GGVF (without any recent improvements).

2 Generalized gradient vector flow snakes

An active contour or snake is a parametric curve $X(s) = (x(s), y(s)), s \in [0, 1]$ evolving inside the image domain, so that it eventually attaches itself to the boundary of the object of interest.

Derived from the corresponding energy functional [53], the evolution of the snake is governed by Euler equations given by

$$a\frac{d^2X}{ds^2} + b\frac{d^4X}{ds^4} + \nabla E_{\text{ext}} = 0,$$

where the weighting parameters a and b control the snake's tension and rigidity and ∇E_{ext} is the generalized gradient vector flow (GGVF) [56] defined as the equilibrium solution of the following system of partial derivative equations

$$\frac{\partial V}{\partial t} - g(|\nabla f|)\nabla^2 V - h(|\nabla f|)(\nabla f - V) = 0,$$

where f is the image gray level, $g(|\nabla f|) = e^{-(|\nabla f|/K)}$, $h(|\nabla f|) = 1 - g(|\nabla f|)$, and K is a calibration parameter.
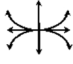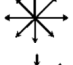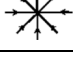
3 Phase portrait analysis

The idea to use the phase portrait for oriented patterns [111] in image processing has been used in fingerprint identification [109, 113], texture analysis [112] and satellite imagery [107, 108]. In particular, phase portrait techniques have been applied to detect architectural distortions in mammogram breast images [114]. However, to the best

of our knowledge, PPA for initialization of the GGVF snakes has been overlooked. PPA is based on the analysis of the critical points of the vector flow assumed to change linearly in the neighborhood of the critical point as follows, $v = Ap$, where p is the Cartesian coordinate and A is the corresponding matrix. The flow patterns characterized by the eigenvalues of matrix A are shown in Table 1, where λ_1, λ_2 are the eigenvalues, $R_i = \text{Re}\lambda_1$, and $I_i = \text{Im}\lambda_i$ [115, 116]. The proposed vector field classifier employs a continuous formulation given by

$$C(\lambda_1, \lambda_2) = \begin{cases} \dfrac{\min(|\lambda_1|, |\lambda_2|)}{\max(|\lambda_1|, |\lambda_2|)} \dfrac{\text{sign}(\lambda_1\lambda_2) + 1}{2}, & \text{if } \lambda_1 > \delta, \lambda_2 > \delta, \\ 0, & \text{otherwise.} \end{cases}$$

(1)

Table 1 PPA: attracting and repelling stars

Pattern	Eigenvalues		Illustration
Saddle point	$R_1 > 0, R_2 < 0$	$I_1 = I_2 = 0$	
Repelling node	$R_1 \neq R_2 > 0$	$I_1 = I_2 = 0$	
Attracting node	$R_1 \neq R_2 < 0$	$I_1 = I_2 = 0$	
Repelling star	$R_1 = R_2 > 0$	$I_1 = I_2 = 0$	
Attracting star	$R_1 = R_2 < 0$	$I_1 = I_2 = 0$	

where δ is a threshold to exclude ill-conditioned matrices characterized by small eigenvalues. The term $\frac{\min(|\lambda_1|, |\lambda_2|)}{\max(|\lambda_1|, |\lambda_2|)}$ includes converging/diverging configurations, i.e., attracting and repelling stars (see Table 1). The term $\frac{\text{sign}(\lambda_1\lambda_2) + 1}{2}$ excludes the saddle points. All other patterns get a 0 score. The converging/diverging configurations are differentiated by the sign of the eigenvalues. Since GGVF eventually eliminates small groups of noisy pixels, the seeds must be initialized around large or medium size stars and nodes. Therefore, the PPA is combined with a growing window as follows: If $\left(C(\lambda_1, \lambda_2)_k > \Delta\right)$, $\lambda_1 > 0, \lambda_2 > 0$, for every $k = k_1, \ldots, k_2$, where k is the size of the growing window and Δ is the suitable threshold to detect the large configuration, then the window is a candidate to be the seed.

The seed windows are then covered by the initial snakes in order to exclude the false boundaries and artifacts.

4 The algorithm

The algorithm is based on the idea that if we detect all the converging and diverging stars *inside* the object and run the expanding snakes from them, they will eventually merge and attach themselves to the boundary (in case of attracting star, the vector field must be inverted). Let N_D and N_C be the number of the diverging and converging stars, respectively. The first stage of the algorithm is then given by the following pseudo-code:

void Evolve_the_Snakes(int i**)**
{ Initialize a snake S_i around the diverging star D_i. The snake is initialized as a circle inside the maximum window satisfying $C(\lambda_1, \lambda_2)_k > \Delta$.

Evolve S_i until it converges. If S_i touches the image boundary, smooth the vector field inside the resulting contour.

Exclude D_i from the set of the diverging stars.
}
void Process_VectorField(void)
{ **do**
  { **Detect_all_Diverging_Stars** D_i *//use classifier (1)*

    Evolve_the_Snakes (N_D) *// call Evolve_the_Snakes N_D times*
  }**while** the number of diverging stars does not change and every snake converges to the same position.
}
void main(void)*// the program body*
{ **do**
  { **Process_VectorField()**
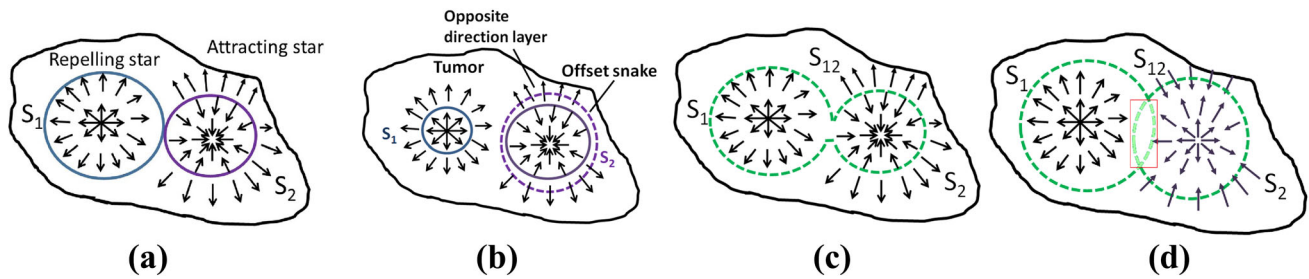   **Invert_the_vector_field** *//The converging stars become diverging.*
   Process_VectorField()
  }**while** every S_i does not converge to the same position.
}

Fig. 2 a Snake growing from a converging configuration "wakes up" a "sleeping" snake, **b** the offset snake picks up the opposite direction of the vector field, **c** merging of the growing contours, **d** merging of the intersecting contours

The algorithm is illustrated in Figs. 1 and 2. The first stage eliminates the seeds positioned outside the object. If a snake reaches the image boundary, the algorithm smoothens the vector field inside the contour to give the way to the snakes, which would have been blocked otherwise. The iterative procedure eventually excludes every external star (converging or diverging) leaving the internal stars intact (see Fig. 1). When the vector field gets inverted, e.g., $V_{\text{inverted}} = -V$, the converging snakes become diverging, so that they are grown on V_{inverted} until they meet vectors in the opposite direction. When they stop, they get offset and then are grown further on the original vector field.

Note that at the first stage, merging is not allowed: If the external and internal snakes merge, the tumor becomes undetectable (see Fig. 1a–c). However, when the external snakes disappear, merging becomes the basic mechanism of the proposed initialization. The algorithm runs on the original vector field where the converging snakes are considered "sleeping," whereas the diverging snakes are growing and merging. Snakes S_1, S_2 merge whenever $\text{dist}_{H_1}(S_1, S_2) < \delta$, where δ is the merging threshold and dist_{H_1} is the Hausdorff distance (see the definition in Sect. 5). It is often the case that a growing snake merges with the "sleeping" snake and the resulting contour keeps growing (Fig. 2a). However, the algorithm does not guarantee that. Therefore, the converging snakes, which have not been "woken up," are offset by several pixels to pick up the repelling component of the vector field (Fig. 2b). Note that for the converging configuration the small offset never intersects the boundary, since there is always a layer of vectors toward the boundary (Fig. 2a). The merging procedure generates a joint growing contour when the snakes are at the distance less or equal to δ (Fig. 2c) or when the snakes intersect due to initialization or due to excessive numerical step (overstepping). The algorithm includes detection of intersections and performs tracing to generate a joint contour, which becomes a new snake (Fig. 2d). The topological changes follow conventional split-and-merge procedures [76, 117, 118]. Besides, our split-and-merge algorithm has been successfully tested on complex-shaped objects in [119].

Note that expanding from the inside of the object is not mandatory. In some cases, it is acceptable to clean up all the converging and diverging configurations outside the object and initialize contracting snake from the image boundary. However, the tumor generally has some homogeneity properties. Second, even though the smoothing process erases the attracting and repelling stars, the resulting vector field outside the tumor still could be chaotic and include false boundaries.

5 Numerical experiments

Our numerical experiments have been performed on 40 synthetic images, subjected to various levels of noise, and on 15 real US images of breast cancer. The method has been compared with a quasi-automatic initialization [96, 97] based on detection of the centers of the weak and strong divergences. A special tracing procedure connects them, generating some kind of skeleton of the object. The skeleton snake requires one manually defined point inside the object (not fully automatic), whereas our procedure runs in an entirely automatic mode. Moreover, the skeleton snake has not been properly tested against a series of real images. The impact of the noise was not evaluated, and the accuracy of the segmentation has not been estimated. In this section, we show that skeleton initialization is sensitive to the noise and PPA outperforms this method in terms of the number of correct initializations and the accuracy.

We also compare the proposed initialization method equipped only with a basic version of GGVF with the adaptive diffusion flow (ADF) [66], a recent version of the level set method (LSM) [37, 38] and an advanced version of the fuzzy C-mean clustering (FCM) [39, 40]. The proposed method outperforms the above algorithms even though we use the most basic GGVF (without any recent improvements).
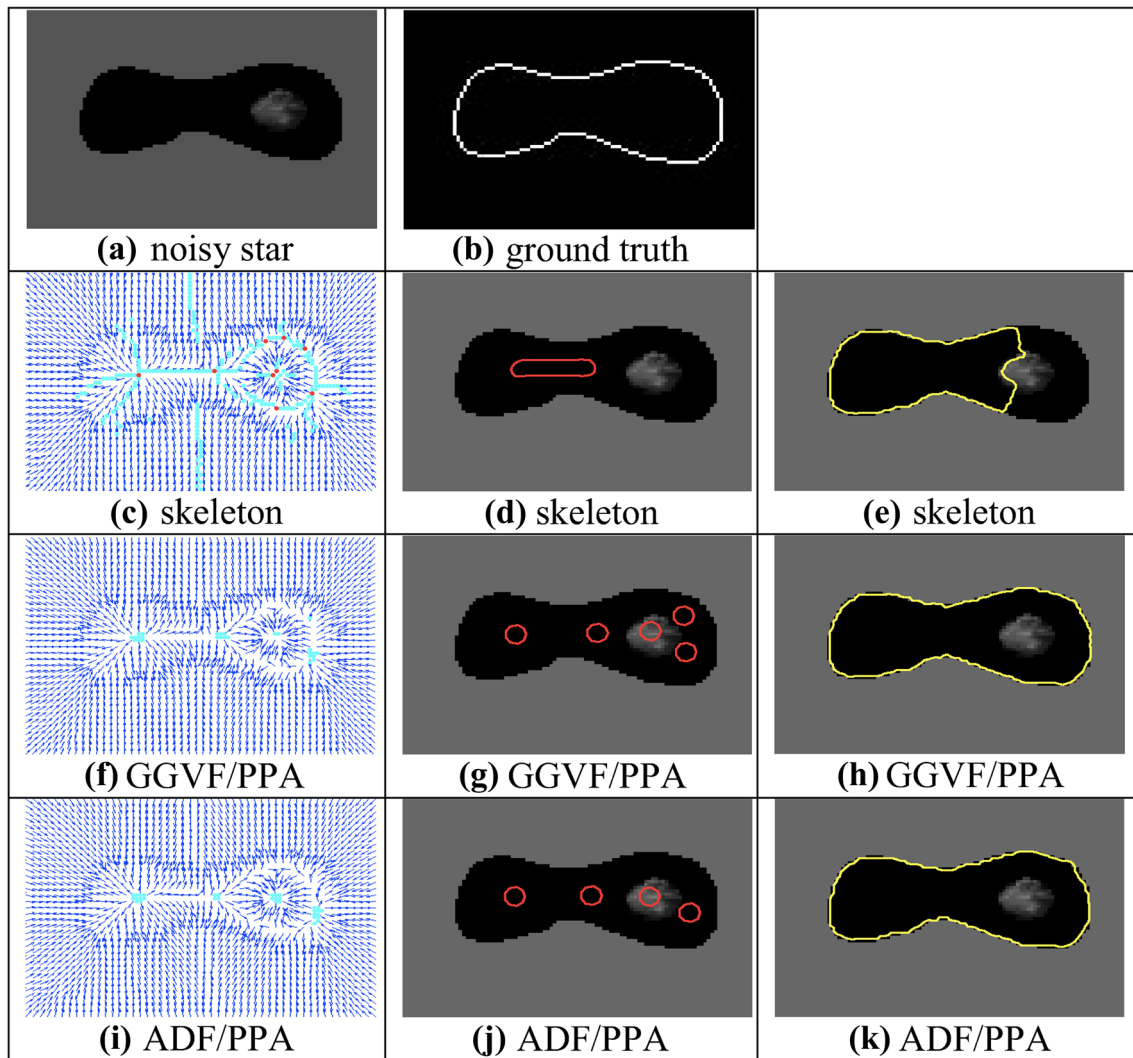
Fig. 3 Skeleton vs. PPA initialization, introductory example: **a** a synthetic tumor, **b** the ground truth, **c** skeleton snake: strong and weak diverging points, **d** skeleton initialization, **e** skeleton snake: final contour, **f** GGVF and the corresponding stars, **g** PPA initialization, **h** PPA: final contour, **i** ADF and the corresponding stars, **j** ADF/PPA initialization, **k** ADF/PPA snake: final contour

The accuracy is measured by the Hausdorff distance between the resulting contour and the ground truth, by the percentage of true positives (TP) as well as by the specificity (SPE), sensitivity (SEN) and accuracy (ACC). To compare the method with the skeleton snakes, we also use a binary measure counting the number of times when the initial snakes were correctly initialized inside the tumor. This allows to evaluate the true accuracy since an incorrect initialization can substantially decrease the average accuracy. On the other hand, even a correct initialization does not mean a good accuracy. Figure 3a–e is an introductory example showing the skeleton initialization getting "distracted" by the inside converging configurations such a noisy "star" located nearby the boundary (cf. correct segmentation by the PPA in Fig. 3f–k). Furthermore, even when the initialization is correct,

i.e., positioned inside the tumor, it does not guarantee that the algorithm reaches the boundary. Figure 4 shows that the ADF, LSM and FCM may fail if the seed is initialized in a noisy area.

Finally, Fig. 5 shows an example from Tauber et al. [96]. PPA and the skeleton segmentations are practically identical; however, the skeleton snake requires one manually defined internal point, whereas PPA performs in an entirely automatic mode.

5.1 Example 1: synthetic images

Forty (300 × 200) images of synthetic tumors were generated by using oval-like shapes subjected to elastic deformations [120] and a trigonometric boundary noise
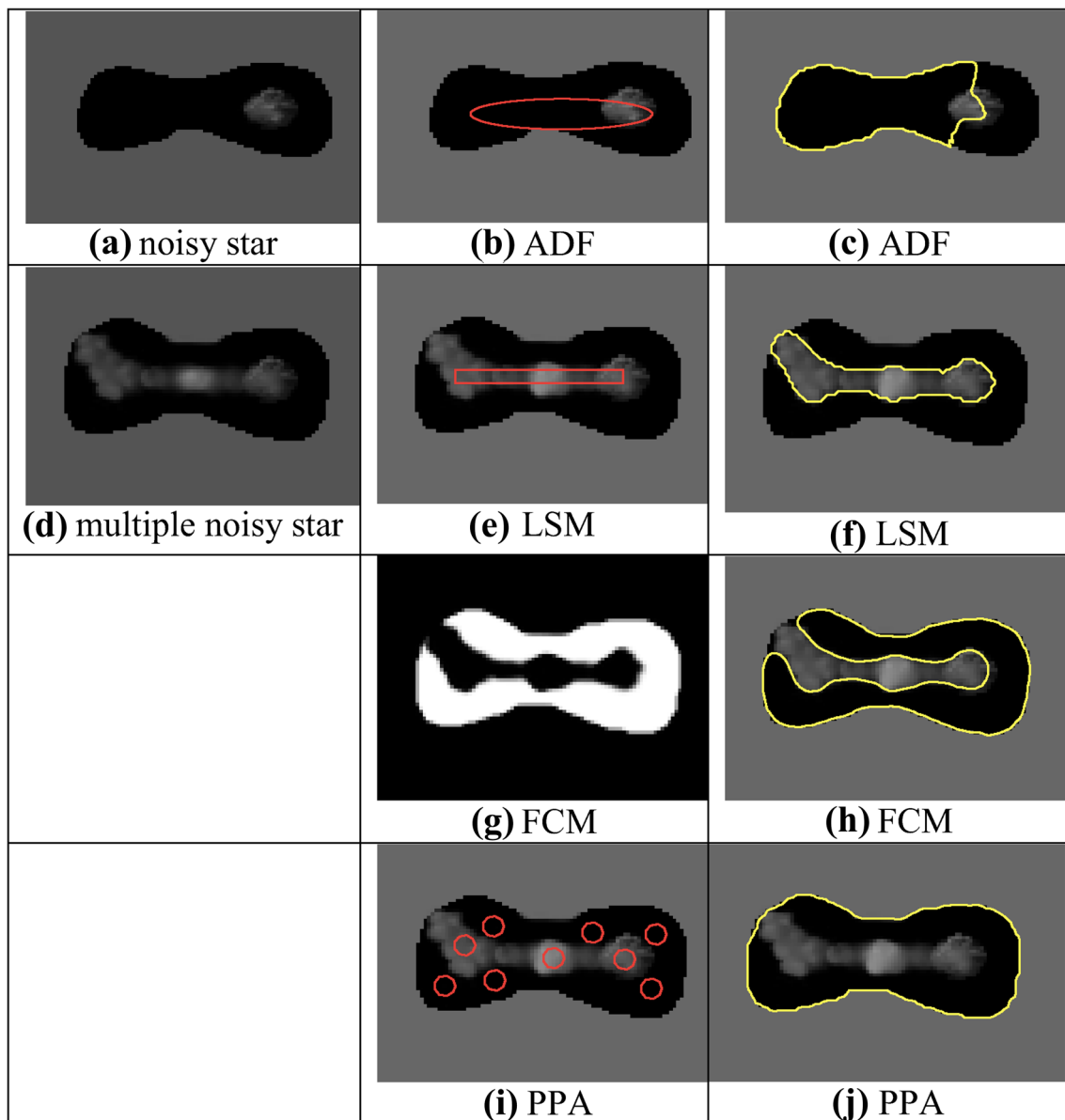
Fig. 4 Introductory example PPA vs. ADF, LSM and FCM: **a** noisy star, **b** ADF, manual initialization, **c** ADF, manual initialization: final contour, **d** multiple noisy star, **e** LSM manual initialization, **f** LSM: the final contour, **g** FCM clustering, **h** FCM: final contour, **i**, **j** PPA solution for the multiple noisy star
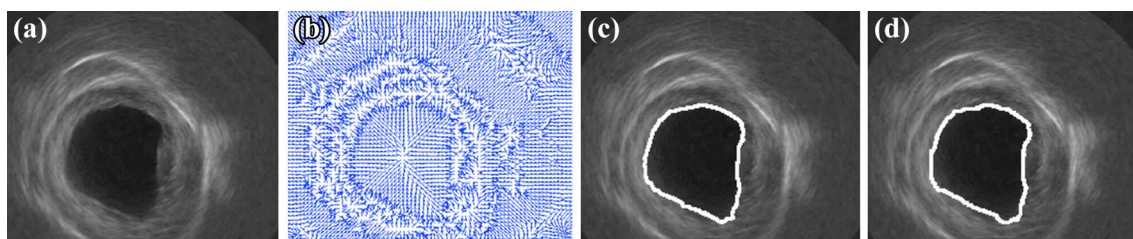
Fig. 5 **a** US image from [96], **b** the vector field, **c** PPA segmentation, **d** Tauber's segmentation

(Fig. 6). The images were degraded by the impulse noise and the additive speckle noise (30–20 dB). The images are characterized by a low contrast $c = \frac{G_{out} - G_{in}}{G_{out}} = 0.51$, where G_{in}, G_{out} is the average gray level inside and outside the tumor. Figure 6 shows an example of a typical synthetic image subjected to the speckle noise.

Fig. 6 Synthetic tumors subjected to impulse and speckle noise

| | 0 dB | 30dB | 26dB | 21dB |
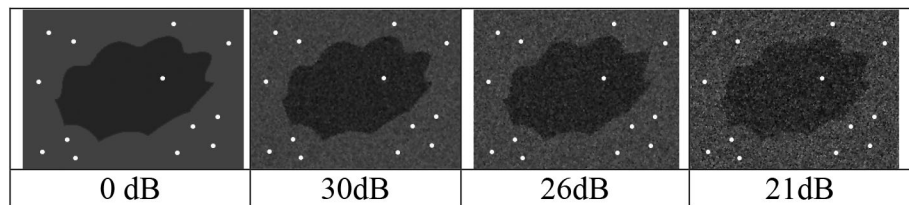
Table 2 PPA versus benchmark methods

Noise, dB	Model	Correctly initialized inside object, % images	Correctly segmented, % images	Accuracy						
				Contour-based evaluation				Region-based evaluation		
				H_1	H_2	H_3	TP	SEN	SPE	ACC
0	PPA + GGVF	100	**100**	**2.10**	**0.73**	1.67	99.95	**99.80**	99.06	**99.33**
	Skeleton + GGVF	80	40	63.92	23.09	26.57	80.16	82.78	99.15	91.50
	PPA + ADF	100	**100**	2.13	0.74	**1.57**	**100.00**	99.74	99.11	**99.33**
	LSM	Manual	80	12.46	5.49	3.32	79.91	81.25	99.59	94.97
	FCM	Manual	80	12.46	5.47	27.71	79.96	80.80	**99.93**	99.03
	ADF, 60 %	Manual	10	88.91	29.85	36.94	54.73	64.77	99.61	87.68
30	PPA + GGVF	90	**90**	4.15	**1.46**	**2.60**	98.12	**99.32**	99.54	99.33
	Skeleton + GGVF	60	30	103.64	57.18	61.31	68.68	66.92	99.65	**90.38**
	PPA + ADF	90	**90**	**3.79**	1.57	3.16	94.84	98.28	99.71	99.23
	LSM	Manual	80	14.08	6.14	4.09	78.78	80.40	99.96	94.88
	FCM	Manual	80	12.93	5.53	27.71	79.82	80.86	99.88	94.94
	ADF, 60 %	Manual	0	90.44	29.41	36.71	50.79	63.85	**99.89**	87.63
26	PPA + GGVF	80	**80**	**4.53**	**1.67**	**3.23**	**95.37**	**98.56**	99.65	99.24
	Skeleton + GGVF	60	10	104.68	69.82	73.86	52.91	60.03	99.66	85.93
	PPA + ADF	80	**80**	4.66	1.86	3.62	87.53	97.47	99.72	**98.94**
	LSM	Manual	**80**	15.47	6.33	4.30	77.01	79.91	**99.95**	94.69
	FCM + LSM	Manual	**80**	13.31	5.52	27.43	79.38	80.57	99.82	94.90
	ADF, 60 %	Manual	0	94.11	34.35	42.75	44.26	59.93	99.88	86.18
21	PPA + GGVF	80	70	**9.42**	**1.98**	3.56	**88.00**	97.55	99.55	**98.73**
	Skeleton + GGVF	60	10	141.75	136.78	138.19	47.70	52.91	99.59	82.91
	PPA + ADF	80	70	10.56	2.08	**3.51**	83.46	96.78	99.27	98.34
	LSM	Manual	70	19.81	6.67	4.60	71.38	79.10	**99.88**	94.33
	FCM	Manual	80	14.15	5.73	27.92	77.75	79.94	99.73	94.60
	ADF, 60 %	Manual	0	90.65	38.11	48.89	37.26	52.34	99.84	83.16

The bold numbers indicate the best accuracy in each category

Table 2 compares the competing methods in terms of the TP and a Hausdorff distance given by $\text{dist}_{H_1}(X,Y) = \max\{\max_{a\in X}\min_{b\in Y}||a-b||, \max_{b\in Y}\min_{a\in X}||a-b||)$, where $||\,||$ denotes the Euclidean distance, X the ground-truth contour, and Y the resulting contour.

The averaged Hausdorff distance H_2 is obtained from H_1 by replacing the internal maximum by averaging. Finally, the relative Hausdorff distance is given by $\text{dist}_{H_3}(X,Y) = \frac{\text{dist}_{H_1}(X,Y)}{L_Y}\xi$, where L_Y is the length of the true contour, and $\xi = 1000$ is a normalizing coefficient. The image is considered to be correctly segmented if $\text{dist}_{H_1}(X,Y) \le 15$.

However, the average accuracy was evaluated for all cases when the snakes were correctly initialized inside the tumor. The FCM runs with 3 clusters corresponding to the tumor, dark background and white shadow areas. The initial centers of the clusters are the average gray levels in these clusters. Since the FCM is a region-based method, the final contour for evaluating H_1 was generated by the LSM [39, 40]. The initial contours for ADF and LSM were generated manually in the noisy areas of the image. The area of the initial contour was about 60 % of the total area of the tumor. Clearly, the PPA has an overwhelming advantage with regard to skeleton snakes practically for every noise

level. Even in the absence of the speckle noise (but with the impulse noise present), only 80 % of the skeleton snakes are correctly initialized and only half of that 80 % reaches the boundary. As far as the overall performance is concerned, the increasing noise level leads to a further decrease in the accuracy of the skeleton snakes. For instance, in case of 21 dB, only 10 % of the skeleton snakes are successful. The performance of the ADF snake with manual initialization is catastrophic with 0 correct segmentations at 21 db; however, the LSM and FCM are comparable in terms of the number of correctly segmented images; however, PPA is consistently more accurate. Besides, the forthcoming Example 2 shows that PPA overperforms the LSM and FCM in terms of the number of correctly segmented tumors in case of *real* US images.

Finally, combining PPA with the ADF does not lead to a substantial improvement. Moreover, in some cases, PPA/GGVF produces more accurate segmentation. This is because the standard deviation σ of a Gaussian smoother required for the ADF has not been tuned. We do not adjust it deliberately; otherwise, it would not be fair with regard to PPA/GGVF which does not use the Gaussian smoothing at all. We consider $\sigma = 0.5$ as recommended in [66].

5.2 Example 2: ultrasound images of the breast cancer

This section tests the initialization using the PPA snakes against the skeleton snakes on a series of 15 US images of the breast cancer. The images have been obtained from

Philips iU22 ultrasound machine available at Department of Radiology, Thammasat University Hospital. The ROIs have been outlined manually. The ground-truth contours have been hand-drawn by the leading radiologists with Department of Radiology, Faculty of Medicine of Thammasat University. The resolution of the images ranges from 200×200 to 300×400.

Examples which demonstrate the advantages of the PPA snakes applied to the real US images are shown in Figs. 7 and 8. Clearly, the skeleton snakes, ADF, LSM and FCM fail when the tumor includes a large non-homogeneous area characterized by the noise and/or shadows. In this case, the resulting contour may be attracted to false boundaries, whereas PPA avoids the false boundaries using multiple, properly initialized snakes.

Table 3 compares the performance of PPA with the skeleton snakes as well as with LSM, FCM and ADF. The initial contour for ADF and LSM was generated manually in the noisy areas of the image. Clearly, the PPA outperforms the skeleton snakes due to the ability to detect the internal and external stars, avoidance of the noise and the use of multiple seeds, whereas the skeleton seed often grows outside the object or creates an incorrect skeleton which jeopardizes the entire initialization. Furthermore, FCM and ADF are apparent losers (60 and 46 %, respectively). The performance of LSM is somewhat acceptable; however, it segments correctly only 73 % of the images, whereas PPA generates 93 % correct segmentations. Finally, PPA scores the best in 8 categories from 9 (bold-face numbers in Table 3).
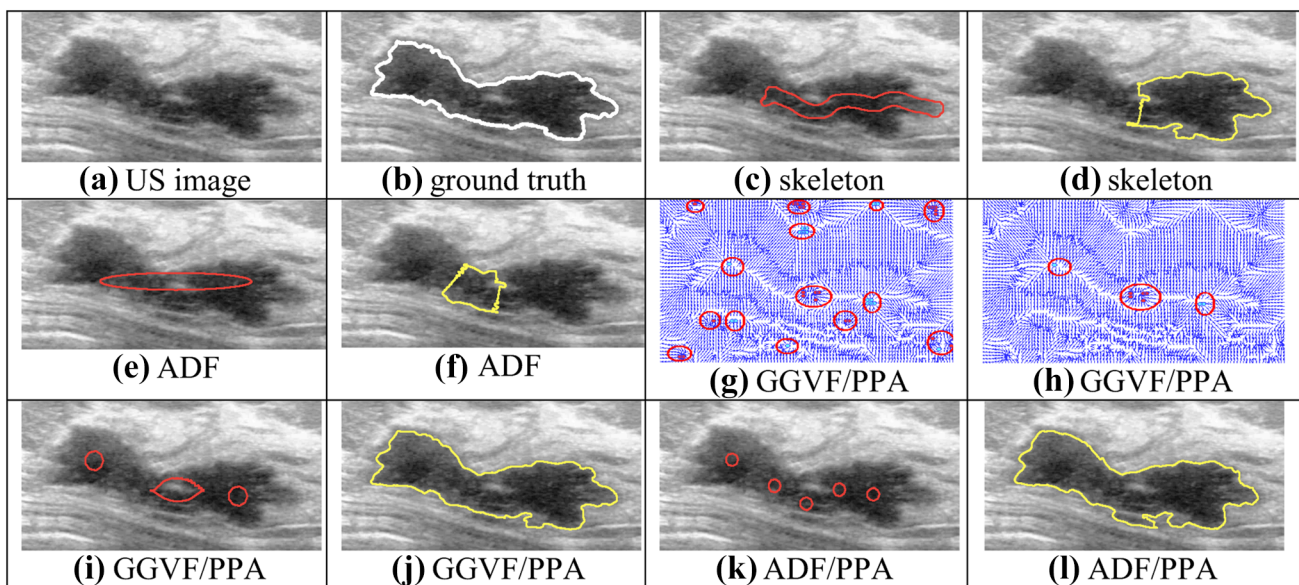
Fig. 7 **a** US image, **b** ground truth, **c** skeleton initialization, **d** skeleton final contour, **e** ADF manual initialization, **f** ADF final contour, **g** GGVF/PPA stars before elimination, **h** GGVF stars after elimination, **i** PPA/GGVF initialization, **j** PPA/GGVF final contour, **k** PPA/ADF initialization, **l** PPA/ADF final contour
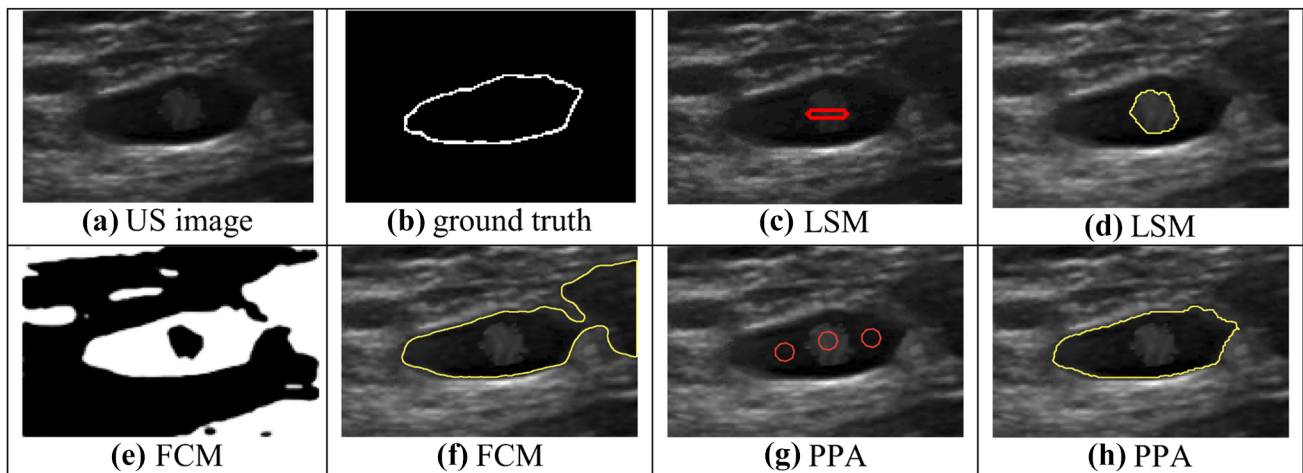
Fig. 8 PPA vs. LSM vs. FCM, **a** US image, **b** ground truth, **c** LSM manual initialization, **d** LSM final contour, **e** FCM clusters, **f** FCM: final contour, **g** PPA initialization, **h** PPA: final contour

Table 3 PPA versus benchmark methods

Model	Correctly initialized inside object, % images	Correctly segmented, % images	Accuracy						
			Contour-based evaluation				Region-based evaluation		
			H_1	H_2	H_3	TP	SEN	SPE	ACC
PPA + GGVF	**100**	**93.33**	**8.64**	**2.16**	3.15	89.66	94.50	99.67	**98.38**
Skeleton + GGVF	86.67	66.67	19.09	7.02	8.36	79.77	88.94	99.82	97.54
PPA + ADF	100	**93.33**	8.54	2.13	**3.07**	**92.58**	**94.53**	99.54	98.25
LSM	Manual	73.33	38.81	21.25	22.63	66.81	69.77	99.54	90.11
FCM	Manual	60	25.43	4.93	6.59	76.19	92.10	96.14	95.41
ADF, 60 %	Manual	46.67	47.43	20.36	19.54	68.15	73.34	**99.91**	92.72

The bold numbers indicate the best accuracy in each category

6 Limitations of the method

The algorithm has been designed and implemented for the case of a single object (a malignant or benign tumor in the US images). The case of multiple objects needs further modifications, which lie out of the scope of the paper. Furthermore, in the case of very noisy images characterized by a low contrast, the trial external snake may get stacked inside the image and may not reach the boundary at all. A possible extension is a combination of the proposed multiple growing snakes initialized inside the US image and sequence of contracting balloon snakes [80] initialized at the boundary of the image characterized by a varying balloon force.

7 Conclusions

The proposed automatic procedure for initialization of snakes for segmentation of the US breast cancer images (PPA) shows an excellent performance as applied to

synthetic as well as to real US images and outperforms a recently proposed quasi-automatic method (skeleton snakes). The proposed initialization method equipped with the most basic version of GGVF also outperforms the adaptive diffusion flow, an advanced level set method and a fuzzy C-mean clustering combined with the level set method. The numerical experiments show that in many cases, the benchmark algorithms do not reach the boundary due to inappropriate initial positions of the seeds.

References

1. Ma Z, Tavares JMRS, Jorge RMN (2009) A review on the current segmentation algorithms for medical images. In: Proceedings of the 1st international conference on Imaging Theory and Applications (IMAGAPP), Portugal, pp. 135–140.
2. Noble JA, Boukerroui D (2006) Ultrasound image segmentation: a survey. IEEE Trans Med Imaging 25(8):987–1010

3. Horsch K, Giger ML, Venta LA, Vyborny CJ (2001) Automatic segmentation of breast lesions on ultrasound. Med Phys 28(8):1652–1659

4. Horsch K, Giger ML, Venta LA, Vyborny CJ (2002) Computerized diagnosis of breast lesions on ultrasound. Med Phys 29(2):157–164

5. Horsch K, Giger ML, Vyborny CJ, Venta LA (2004) Performance of computer-aided diagnosis in the interpretation of lesions on breast sonography. Acad Radiol 11(3):272–280

6. Drukker K, Giger ML, Horsch K, Kupinski MA, Vyborny CJ, Mendelson EB (2002) Computerized lesion detection on breast ultrasound. Med Phys 29(7):1438–1446

7. Drukker K, Giger ML, Vyborny CJ, Mendelson EB (2004) Computerized detection and classification of cancer on breast ultrasound. Acad Radiol 11(5):526–535

8. Shan J, Cheng HD, Wang Y (2012) Completely automated segmentation approach for breast ultrasound images using multiple-domain features. Ultrasound Med Biol 38(2):262–275

9. Jiang P, Peng J, Zhang G, Cheng E, Megalooikonomou V, Ling H (2012) Learning-based automatic breast tumor detection and segmentation in ultrasound images. In: the 9th IEEE international symposium biomedical imaging (ISBI), pp. 1587–1590

10. Jesneck JL, Lo JY, Baker JA (2007) Breast mass lesions: computer-aided diagnosis models with mammographic and sonographic descriptors. Radiology 244(2):390–398

11. Chen CM, Chou YH, Han KC, Hung GS, Tiu CM, Chiou HJ, Chiou SY (2003) Breast lesions on sonograms: computer-aided diagnosis with nearly setting-independent features and artificial neural networks. Radiology 226(2):504–514

12. Song JH, Venkatesh SS, Conant EF, Cary TW, Arger PH, Sehgal CM (2005) Artificial Neural Network to aid differentiation of malignant and benign breast masses by ultrasound imaging. In: Proceedings of SPIE, progress in biomedical optics and imaging, pp.148–152

13. Joo S, Yang YS, Moon WK, Kim HC (2004) Computer-aided diagnosis of solid breast nodules: use of an artificial neural network based on multiple sonographic features. IEEE Trans Med Imaging 23(10):1292–1300

14. Huang YL, Wang KL, Chen DR (2005) Diagnosis of breast tumors with ultrasonic texture analysis using support vector machines. Neural Comput Appl 15(2):164–169

15. Huang YL, Chen DR (2004) Watershed segmentation for breast tumor in 2-D sonography. Ultrasound Med Biol 30(5):625–632

16. Xiao G, Brady M, Noble JA, Zhang Y (2002) Segmentation of ultrasound B-mode images with intensity inhomogeneity correction. IEEE Trans Med Imaging 21(1):48–57

17. Boukerroui D, Baskurt A, Noble JA, Basset O (2003) Segmentation of ultrasound images-multiresolution 2D and 3D algorithm based on global and local statistics. Pattern Recognit Lett 24(45):779–790

18. Kannan SR, Devi R, Ramathilagam S, Takezawa K (2013) Effective FCM noise clustering algorithms in medical images. Comput Biol Med 43(2):73–83

19. Son LH, Tuan TM (2016) A cooperative semi-supervised fuzzy clustering framework for dental X-ray image segmentation. Expert Syst Appl 46(C):380–393

20. Zhang X, Li X, Feng Y (2015) A medical image segmentation algorithm based on bi-directional region growing. Optik—Int J Light Electron Optics 126(20):2398–2404

21. Madabhushi A, Metaxas DN (2003) Combining low-, high-level and empirical domain knowledge for automated segmentation of ultrasonic breast lesions. IEEE Trans Med Imaging 22(2):155–169

22. Chen D, Chang R, Wu WJ, Moon W, Wu WL (2003) 3-D breast ultrasound segmentation using active contour model. Ultrasound Med Biol 29(7):1017–1026

23. Chang RF, Wu WJ, Moon WK, Chen WM, Lee W, Chen DR (2003) Segmentation of breast tumor in three-dimensional ultrasound images using three-dimensional discrete active contour model. Ultrasound Med Biol 29(11):1571–1581

24. Chang RF, Wu WJ, Tseng CC, Chen DR, Moon WK (2003) 3-D snake for US in margin evaluation for malignant breast tumor excision using Mammotome. IEEE Trans Inform Technol Biomed 7(3):197–201

25. Sahiner B, Chan HP, Roubidoux MA, Helvie MA, Hadjiiski LM, Ramachandran A, Paramagul C, LeCarpentier GL, Nees A, Blane C (2004) Computerized characterization of breast masses on three-dimensional ultrasound volumes. Med Phys 31(4):744–754

26. Liu Q, Jiang M, Bai P, Yang G (2016) A novel level set model with automated initialization and controlling parameters for medical image segmentation. Comput Med Imaging Graph 48:21–29

27. Chen DR, Chang RF, Kuo WJ, Chen MC, Huang YL (2002) Diagnosis of breast tumors with sonographic texture analysis using wavelet transform and neural networks. Ultrasound Med Biol 28(10):1301–1310

28. Cheng HD, Shan J, Ju W, Guo Y, Zhang L (2010) Automated breast cancer detection and classification using ultrasound images: a survey. Pattern Recognit 43(1):299–317

29. James AP, Dasarathy BV (2014) Medical image fusion: a survey of the state of the art. Inf Fusion 19:4–19

30. Smistad E, Falch TL, Bozorgi M, Elster AC, Lindseth F (2015) Medical image segmentation on GPUs—A comprehensive review. Med Image Anal 20(1):1–18

31. Iglesias JE, Sabuncu MR (2015) Multi-atlas segmentation of biomedical images: a survey. Med Image Anal 24(1):205–219

32. Ghosh P, Mitchell M, Tanyi JA, Hung AY (2016) Incorporating priors for medical image segmentation using a genetic algorithm. Neurocomputing. doi:10.1016/j.neucom.2015.09.123

33. Ma Z, Jorge RN, Tavares JM (2010) A shape guided C–V model to segment the levator ani muscle in axial magnetic resonance images. Med Eng Phys 32(7):766–774

34. Wang J, Yeung S-K, Chan KL (2015) Matching-constrained active contours with affine-invariant shape prior. Comput Vis Image Underst 132:39–55

35. el Diop HS, Burdin V (2013) Bi-planar image segmentation based on variational geometrical active contours with shape priors. Med Image Anal 17(2):165–181

36. Wang B, Gao X, Li J, Li X, Tao D (2015) A level set method with shape priors by using locality preserving projections. Neurocomputing 170:188–200

37. Li C, Xu C, Gui C, Fox MD (2010) Distance regularized level set evolution and its application to image segmentation. IEEE Trans Image Process 19(12):3243–3254

38. Li C. (2006) Level set for image segmentation. Matlab File Exchange MathWorks. http://www.mathworks.com/matlabcentral/fileexchange/12711-level-set-for-image-segmentation Accessed 10 Jan 2016

39. Li BN, Chui CK, Chang S, Ong SH (2011) Integrating spatial fuzzy clustering with level set methods for automated medical image segmentation. Comput Biol Med 41(1):1–10

40. ABing (2011) Spatial fuzzy clustering and level set segmentation. Matlab File Exchange MathWorks. http://www.mathworks.com/matlabcentral/fileexchange/31068-spatial-fuzzy-clustering-and-level-set-segmentation. Accessed 10 Jan 2016

41. Ma Z, Tavares JMRS (2016) A novel approach to segment skin lesions in dermoscopic images based on a deformable model. IEEE J Biomed Health Inform 20(2):615–621

42. Ma Z, Jorge RMN, Mascarenhas T, Tavares JMRS (2013) A level set based algorithm to reconstruct the urinary bladder from multiple views. Med Eng Phys 35(12):1819–1824

43. Ma Z, Jorge RMN, Mascarenhas T, Tavares JMRS (2012) Segmentation of female pelvic cavity in axial T2-weighted MR images towards the 3D reconstruction. Int J Numer Method Biomed Eng 28:714–726

44. Xie X, Wu J, Jing M (2013) Fast two-stage segmentation via non-local active contours in multiscale texture feature space. Pattern Recognit Lett 34(11):1230–1239

45. Krawczyk B, Schaefer G (2014) A hybrid classifier committee for analysing asymmetry features in breast thermograms. Appl Soft Comput 20:112–118

46. Krawczyk B, Schaefer G, Woźniak M (2015) A hybrid cost-sensitive ensemble for imbalanced breast thermogram classification. Artif Intell Med 65(3):219–227

47. Ozdemir A, Ozdemir H, Maral I, Konus O, Yucel S, Isik S (2001) Differential diagnosis of solid breast lesions: contribution of Doppler studies to mammography and gray scale imaging. J Ultrasound Med 20(10):1091–1101

48. Cho N, Jang M, Lyou CY, Park JS, Choi HY, Moon WK (2012) Distinguishing benign from malignant masses at breast US: combined US elastography and color Doppler US—Influence on radiologist accuracy. Radiology 262(1):80–90

49. Berg WA, Cosgrove DO, Doré CJ, Schäfer FKW, Svensson WE, Hooley RJ, Ohlinger R, Mendelson EB, Balu-Maestro C, Locatelli M, Tourasse C, Cavanaugh BC, Juhan V, Stavros AT, Tardivon A, Gay J, Henry JP, Cohen-Bacrie C (2012) Shear-wave elastography improves the specificity of breast US: the BE1 multinational study of 939 masses. Radiology 262(2):435–449

50. Krawczyk B, Filipczuk P (2014) Cytological image analysis with firefly nuclei detection and hybrid one-class classification decomposition. Eng Appl Artif Intell 31:126–135

51. Filipczuk P, Krawczyk B, Woźniak M (2013) Classifier ensemble for an effective cytological image analysis. Pattern Recognit Lett 34(14):1748–1757

52. Krawczyk B, Galar M, Jeleń Ł, Herrera F (2016) Evolutionary undersampling boosting for imbalanced classification of breast cancer malignancy. Appl Soft Comput 38:714–726

53. Kass M, Witkin A, Terzopoulos D (1988) Snakes: active contour models. Int J Comput Vis 1(4):321–331

54. Ji Z, Xia Y, Sun Q, Cao G, Chen Q (2015) Active contours driven by local likelihood image fitting energy for image segmentation. Inf Sci 301:285–304

55. Xu C, Prince JL (1998) Snakes, shapes, and gradient vector flow. IEEE Trans Image Process 7(3):359–369

56. Xu C, Prince JL (1998) Generalized gradient vector flow external forces for active contours. Sig Process 71(2):131–139

57. Tang J (2009) A multi-direction GVF snake for the segmentation of skin cancer images. Pattern Recognit 42(6):1172–1179

58. Wei M, Zhou Y, Wan M (2004) A fast snake model based on non-linear diffusion for medical image segmentation. Comput Med Imaging Graph 28(3):109–117

59. Li B, Acton ST (2007) Active contour external force using vector field convolution for image segmentation. IEEE Trans Image Process 16(8):2096–2106

60. Hsu CY, Chen SH, Wang KL (2003) Active contour model with a novel image force field. In: Proceeding of the conference CVGIP-2003, Taiwan, pp. 477–483

61. Hsu CY, Liu CY, Chen CM (2008) Automatic segmentation of liver PET images. Comput Med Imaging Graph 32(7):601–610

62. Li C, Liu J, Fox MD (2005) Segmentation of external force field for automatic initialization and splitting of snakes. Pattern Recognit 38(11):1947–1960

63. Cheng J, Foo SW (2006) Dynamic directional gradient vector flow for snakes. IEEE Trans Image Process 15(6):1563–1571

64. Jifeng N, Chengke W, Shigang L, Shuqin Y (2007) NGVF: an improved external force field for active contour model. Pattern Recognit Lett 28(1):58–63

65. Zhu G, Zhang S, Zeng Q, Wang C (2010) Gradient vector flow active contours with prior directional information. Pattern Recognit Lett 31(9):845–856

66. Wu Y, Wang Y, Jia Y (2013) Adaptive diffusion flow active contours for image segmentation. Comput Vis Image Underst 117(10):1421–1435

67. Rodtook A, Makhanov SS (2013) Multi-feature gradient vector flow snakes for adaptive segmentation of the ultrasound images of breast cancer. J Vis Commun Image Represent 24(8):1414–1430

68. Li Q, Deng T, Xie W (2016) Active contours driven by divergence of gradient vector flow. Sig Process 120:185–199

69. Malladi R, Sethian J, Vemuri B (1995) Shape modeling with front propagation. IEEE Trans Pattern Anal Mach Intell 17(2):158–171

70. Osher S, Sethian JA (1988) Fronts propagating with curvature dependent speed: algorithms based on Hamilton-Jacobi formulation. J Comput Phys 79:12–49

71. Caselles V, Kimmel R, Sapiro G (1997) Geodesic active contours. Int J Comput Vis 22(1):61–79

72. Siddiqi K, Lauzie're YB, Tannenbaum A, Zucker SW (1998) Area and length minimizing flows for shape segmentation. IEEE Trans Image Process 7(3):433–443

73. Wang X, He L, Wee WG (2004) Deformable contour method: a constrained optimization approach. Int J Comput Vis 59(1):87–108

74. He L, Peng Z, Everding B, Wang X, Han CY, Weiss KL, Wee WG (2008) A comparative study of deformable contour methods on medical image segmentation. Image Vis Comput 26:141–163

75. Xu C, Pham D, Prince J (2000) Image segmentation using deformable models, In: Beutel JM, Fitzpatrick JM (eds) Handbook of Medical Imaging vol 2: Medical Image Processing and Analysis. SPIE Press, Bellingham, Washington, USA pp. 129–174

76. McInerney T, Terzopoulos D (2000) T-snakes: topology adaptive snakes. Med Image Anal 4(2):73–91

77. Shih FY, Zhang K (2007) Locating object contours in complex background using improved snakes. Comput Vis Image Underst 105:93–98

78. Mille J (2009) Narrow band region-based active contours and surfaces for 2d and 3d segmentation. Comput Vis Image Underst 113:946–965

79. Cohen LD, Cohen I (1993) Finite-element methods for active contour models and balloons for 2-D and 3-D images. IEEE Trans Pattern Anal Mach Intell 15(11):1131–1147

80. Cohen LD (1991) On active contour models and balloons. CVGIP: Image Understanding 53(2):211–218

81. Zhu SC, Yuille A (1996) Region competition: unifying snakes, region growing, and Bayes/MDL for multiband image segmentation. IEEE Trans Pattern Anal Mach Intell 18:884–900

82. Shang Y, Yang X, Zhu L, Deklerck R, Nyssen E (2008) Region competition based active contour for medical object extraction. Comput Med Imaging Graph 32(2):109–117

83. Fenster SD, Kender JR (2001) Sectored snakes: evaluating learned energy segmentations. IEEE Trans Pattern Anal Mach Intell 23(9):1028–1034

84. Fenster A, Tong S, Cardinal HN, Blake C, Downey DB (1998) Three-dimensional ultrasound imaging system for prostate cancer diagnosis and treatment. IEEE Trans Instrum Meas 47(6):1439–1447

85. Jumaat AK, Wan Abdul Rahman WEZ, Ibrahim A, Mahmud R (2010) Segmentation of masses from breast ultrasound images using parametric active contour algorithm. Procedia—Social and Behavioral Sciences 8:640–647

86. Cvancarova M, Albresgtsen F, Brabrand K, Samset E (2005) Segmentation of ultrasound images of liver tumors applying snake algorithms and GVF. Congr Ser 1281:218–223

87. Alemán-Flores M, Alemán-Flores P, Álvarez-León L, Esteban-Sánchez MB, Fuentes-Pavón R, Santana-Montesdeoca JM (2005) Computerized ultrasound characterization of breast tumors. Int Congr Ser 1281:1063–1068

88. Hamarneh G, Gustavsson T (2000) Combining snakes and active shape models for segmenting the human left ventricle in echocardiographic images. In: Computers in cardiology, Cambridge, MA, pp. 115–118

89. Chen CM, Lu HHS, Lin YC (2000) An early vision-based snake model for ultrasound image segmentation. Ultrasound Med Biol 26(2):273–285

90. Mignotte M, Meunier J (2001) A multiscale optimization approach for the dynamic contour-based boundary detection issue. Comput Med Imaging Graph 25(3):265–275

91. Rodtook A, Makhanov SS (2010) Continuous force field analysis for generalized gradient vector flow field. Pattern Recognit 43(10):3522–3538

92. Ma Z, Tavares JMRS, Jorge RMN, Mascarenhas T (2010) A review of algorithms for medical image segmentation and their applications to the female pelvic cavity. Comput Methods Biomech Biomed Eng Imaging Vis 13(2):235–246

93. Ma Z, Jorge RMN, Mascarenhas T, Tavares JMRS (2011) Novel approach to segment the inner and outer boundaries of the bladder wall in T2-weighted magnetic resonance images. Ann Biomed Eng 39(8):2287–2297

94. Ma Z, Jorge RMN, Mascarenhas T, Tavares JMRS (2013) Segmentation of female pelvic organs in axial magnetic resonance images using coupled geometric deformable models. Comput Biol Med 43(4):248–258

95. Rochery M, Jermyn IH, Zerubia J (2006) Higher order active contours. Int J Comput Vis 69:27–42

96. Tauber C, Batatia H, Ayache A (2010) Quasi-automatic initialization for parametric active contours. Pattern Recognit Lett 31(1):83–90

97. Tauber C, Batatia H, Ayache A (2005) A general Quasi-automatic initialization for Snakes: application to ultrasound images. In: Proceedings of international conference on image processing, pp. 806-809

98. Xingfei G, Jie T (2002) An automatic active contour model for multiple objects. In: Proceedings of international conference on pattern recognition, 2, pp. 881–884

99. Hsua CY, Wang HF, Wang HC, Tseng KK (2012) Automatic extraction of face contours in images and videos. Future Gener Comput Syst 28:322–335

100. Veronesea E, Stramarec R, Campiona A, Raffeinerb B, Beltramec V, Scagliori E, Coranc A, Ciprianb L, Fioccob U, Grisana E (2013) Improved detection of synovial boundaries in ultrasound examination by using a cascade of active-contours. Med Eng Phys 35:188–194

101. Doshi DJ, March DE, Crisi GM, Coughlin BF (2007) Complex cystic breast masses: diagnostic approach and imaging-pathologic correlation. Radiographics 27:53–64

102. Jung IS, Thapa D, Wang GN (2005) Automatic segmentation and diagnosis of breast lesions using morphology method based on ultrasound. In: Wang L, Jin Y (ed) Proceedings of international conference on fuzzy systems and knowledge discovery (FSKD), LNAI 3614, pp. 1079–1088

103. Selvan S, Shenbagadevi S (2015) Automatic seed point selection in ultrasound echography images of breast using texture features. Biocybern Biomed Eng 35(3):157–168

104. Fergani K, Lui D, Scharfenberger C, Wong A, Clausi DA (2014) Hybrid structural and texture distinctiveness vector field convolution for region segmentation. Comput Vis Image Underst 125:85–96

105. Liu S, Peng Y (2012) A local region-based Chan-Vese model for image segmentation. Pattern Recognit 45:2769–2779

106. Akgul YS, Kambhamettu C, Stone M (1998) Extraction and tracking of the tongue surface from ultrasound image sequences. In: Proceedings of IEEE Computer Society conference computer vision and pattern recognition, pp. 298–303.

107. Cohen I, Herlin I (1995) A motion computation and interpretation framework for oceanographic satellite images. In: Proceedings of international symposium computer vision, pp. 13–18

108. Cohen I, Herlin I, Rocquencourt I (1996) Optical flow and phase portrait methods for environmental satellite image sequences. In: Proceedings of the 4th European conference on computer vision 2, pp. 141–150.

109. Li J, Yau WY, Wang H (2008) Combining singular points and orientation image information for fingerprint classification. Pattern Recognit 41:353–366

110. Li J, Yau WY, Wang H (2006) Constrained nonlinear models of fingerprint orientations with prediction. Pattern Recognit 39:102–114

111. Shu CF, Jain RC (1994) Vector field analysis for oriented patterns. IEEE Trans Pattern Anal Mach Intell 16:946–950

112. Tian X, Samarasinghe S, Murphy G (1999) An integrated algorithm for detecting position and size of knots on logs using texture analysis. In: Proceedings of conference on image and visions computing, pp. 121–132

113. Yau WY, Li J, Wang H (2004) Nonlinear phase portrait modeling of fingerprint orientation. In: Proceedings of international conference on control, automation, robotics and vision (ICARCV2004 8th), pp. 1262–1267.

114. Rangayyan R, Ayres F (2006) Gabor filters and phase portraits for the detection of architectural distortion in mammograms. Med Biol Eng Comput 44:883–894

115. Jordan D, Smith P (2007) Nonlinear ordinary differential equations: An introduction for scientists and engineers, 4th edn. Oxford University Press, Oxford

116. Chucherd S, Rodtook A, Makhanov SS (2010) Phase portrait analysis for multiresolution generalized gradient vector flow. IEICE Trans Inf Syst E93-D:2822–2835

117. Ngoi KP, Jia JC (1999) An active contour model for colour region extraction in natural scenes. Image Vis Comput 17(13):955–966

118. Choi W, Lam K, Siu W (2001) An adaptive active contour model for highly irregular boundaries. Pattern Recognit 34:323–331

119. Nakaguro Y, Dailey MN, Marukatat S, Makhanov SS (2013) Defeating line-noise CAPTCHAs with multiple quadratic snakes. Comput Secur 37:91–110

120. Jain AK, Zhong Y, Lakshmanan S (1996) Object matching using deformable templates. IEEE Trans Pattern Anal Mach Intell 18:267–278